Available online at www.garmian.edu.krd

Passer Journal

Passer 7 (Issue 1) (2025) 62-69

Original Article

Bio-Inspired Synthesis of Hematite α-Fe_2O_3 Nanoparticles via Rosemary Leaf Extract: Investigation of Structural, Magnetic, and Electrical Properties

Ruqia Flayah[1], Tahseen Mubarak[1], Bruska Azhdar[*2], Zeen Zaki[3]

[1]*Department of Physics, College of Science, Diyala University, Diyala, Iraq.*
[2] *Nanotechnology Research Laboratory, Department of Physics, College of Science, University of Sulaimani, Sulaimani, Iraq.*
[3]*Azmar College for Gifted Students, Sulaimani Directorate of Education, Sulaimani, Iraq.*

Received 8 January 2025; revised 2 February 2025;
accepted 10 February 2025; available online 15 February 2025

DOI: 10.24271/PSR.2025.498695.1890

ABSTRACT

Green synthesis is an eco-friendly, low-toxicity, and cost-effective method for the synthesis of nanoparticles. This study investigates the biosynthesis of hematite α-Fe_2O_3 nanoparticles using rosemary leaf extract as a natural reducing and stabilizing agent, focusing on the influence of pH (3, 7, and 11) on their structural, morphological, magnetic, and electrical properties. X-ray diffraction was employed to confirm the phase and crystallinity of the nanoparticles and revealed that all samples exhibited the hexagonal structure of hematite. Crystallite size calculations using Scherrer's equation showed that size decreased with increasing pH. The largest crystallites were observed at pH 3, indicating faster growth in acidic conditions. Smaller crystallites had higher surface area and porosity. The Fourier-transform infrared spectroscopy confirms the presence of hematite nanoparticles by showing strong peaks below 600 cm^{-1}, which represent the stretching vibrations of Fe-O bonds. Field Emission Scanning Electron Microscopy analysis revealed that the morphology and size of the hematite nanoparticles varied with pH. The nanoparticles synthesized at pH 3 exhibited an aggregated nanoplate shape, while those at higher pH values (7 and 11) resulted in more semi-spherical morphology. The magnetic characteristics were analyzed using Vibrating Samples Magnetometer, which revealed weak ferromagnetic behavior for all pH value. Additionally, the variations in dielectric constant, dielectric loss factor, and conductivity with frequency were studied using an LCR meter.

Keywords: Green synthesis, α-Fe_2O_3 nanoparticles, rosemary leaf extract, VSM, RLC.

1 Introduction

In recent years, nanotechnology has grown in popularity across the board of scientific and technological communities because of its numerous useful applications in engineering, chemistry, medicine, and electronics. Currently, a variety of chemical, physical, and biological methods are used to synthesize metallic nanoparticles [1]. Nanoparticles can be produced through physical and chemical processes; however, these methods are costly and may pose environmental risks [2]. The biological method, which is offered as an alternative to chemical and physical methods, is a less harmful way to synthesize nanoparticles; additionally, this process does not require any hazardous, costly, or poisonous chemicals. This synthesis process can be performed using fungi, algae, bacteria, and plants [3].The synthesis of plant-based nanoparticles involves the combination of a metal salt and a plant extract; the chemical reaction can be completed at room temperature within minutes to a few hours [4]. The various factors that affect plant leaf extracts, including the concentration and type of phytochemicals present, pH level, temperature, and metal salt concentration, all contribute to the variability in nanoparticle production rate, yield, and stability. Extract of plant leaves Phytochemicals exhibit an extraordinary capacity to reduce metal ions at a much faster rate than fungi and bacteria, which necessitate lengthier incubation times. Consequently, plant leaf extracts that are extracted from plant leaves are considered a secure and valuable resource for the synthesis of metal and metal oxide nanoparticles [5].

Metallic nanoparticles with various forms, sizes, and compositions, and physicochemical properties can be synthesized using biological techniques, which have become popular in recent years [6]. Green nanotechnologies for the fabrication of iron-oxide nanoparticles have recently gained in popularity due to their

* Corresponding author
E-mail address bruska.azhdar@univsul.edu.iq (Instructor).
Peer-reviewed under the responsibility of the University of Garmian.

applications in biomedicine, cosmetics, bioremediation, diagnostics, and materials engineering. Iron oxide nanoparticles have become increasingly important due to their environmentally friendly nature, catalytic activity, and low cost [7]. Iron oxide crystallites consist of different phases: hematite (α-Fe_2O_3), maghemite (γ-Fe_2O_3), and magnetite (Fe_3O_4) [8]. Iron oxide has been gaining popularity because it has unique electrical, optical, and magnetic properties that can be used in numerous applications, including the production of inorganic pigments, magnetic storage media, gas sensors, electronic and optical devices, information storage, magneto caloric refrigeration, bioprocessing, ferrofluid technology, and wastewater treatment adsorbents [9]. The iron oxide nanoparticles have a great attraction in biomedical applications due to their non-toxic role in the biological systems [10].

Different synthesis methods to produce hematite nanoparticles have been documented in the literature, including green synthesis, hydrolysis, hydrothermal, precipitation, solvothermal, combustion, facile solution, sol-gel, and microemulsion approaches [11]. Among these methods, green synthesis offers an environmentally friendly, low-toxicity, cost-effective, and efficient method for synthesizing and fabricating nanoparticles[12]. Iron oxide nanoparticles were synthesized using a variety of plant extracts, including green tea, pomegranate, grape leaves, and carob leaves [13]. Nowadays, researchers have turned to biological methods of the synthesis of nanoparticles as a preferred alternative method compared to chemical and physical methods due to the accumulation of intra- or extra-cellular inorganic materials in both unicellular and multicellular organisms [14, 15].

The present study examines the synthesis of hematite (α-Fe_2O_3) nanoparticles using rosemary leaf extract in detail. And determined how hydrogen potential influences on the size, shape, and structural properties. X-ray diffraction (XRD) was employed to analyze and confirm the crystalline structural characteristics, and The Fourier-transform infrared spectroscopy (FTIR) examination was subsequently conducted to assess the changes in functional groups of the resulting nanoparticles. Field Emission Scanning Electron Microscopy (FE-SEM) was utilized to examine the shape and particle size distribution. Vibrating Samples Magnetometer (VSM) was employed to assess the magnetic characteristics of the α-Fe_2O_3 nanoparticle, whereas an RLC meter was utilized to evaluate the electrical properties.

2 Material and methods

2.1 Preparation of Rosemary Extract

The fresh leaves of rosemary plants were collected and washed multiple times with tap water to remove grime and surface-adherent materials. Subsequently, they were rinsed with double-distilled water, and dried in our laboratory for one week. Dried rosemary leaves were pulverized in a blender to produce a fine powder of a uniform size. 50 g of powder were added to 1L of distilled water and heated at 60 °C for 1 h, and mixed under ultrasonic for 15 min. The resulting extract was filtered using a filter cloth and centrifuged for 20 min to wash the nanoparticles. For all the experiments, the extract was freshly prepared.

2.2 Synthesis of Iron oxide α-Fe2O3 Nanoparticles

The Rosemary extracts were added to 0.1 M of iron (III) sulfate ($Fe_2(So_4)_3 \cdot xH_2O$) at a volume ratio of 2:1, which was purchased from Biochem Chemopharma. The mixture was stirred with a magnetic stirrer, and ammonia was added to the mixture solution to adjust the pH to 3, 7 and 11, with continued mixing for 2 h. The solution was dried in an oven at 70 °C. Consequently, the powder was annealed at temperatures of 750 °C for 2 hours.

3 Results and discussion

3.1 Structural characterization

X-ray diffraction was employed to investigate the crystalline phase of the hematite (α-Fe_2O_3) nanoparticles. The peaks in the pattern are matched with the JCPDS-ICDD card number 98-006-6756, indicating that they belong to the hexagonal crystal system with space group $R\bar{3}c$ (167). The X-ray diffraction patterns of all prepared samples for pH 3, 7, and 11, annealed at a temperature of 750°C, are shown in Figure 1.

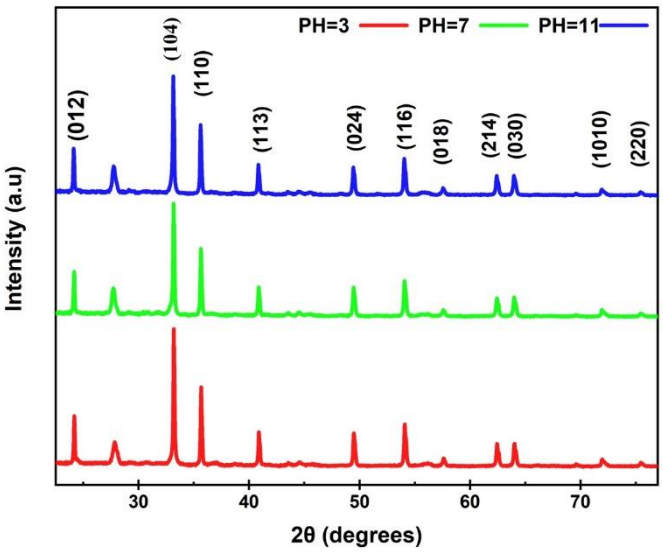

Figure 1: X-ray diffraction pattern of Hematite NPs at pH 3, 7, and 11.

The lattice parameters (a, c) and the volume of the unit cell (V) can be derived from the inter-planar spacing d_{hkl} and the Miller indices (hkl) using these relations [16]:

$$\frac{1}{{d_{hkl}}^2} = \left[\frac{4}{3}\left(\frac{h^2 + hk + k^2}{a^2}\right) + \frac{l^2}{c^2}\right] \quad (1)$$

$$v = \frac{\sqrt{3}}{2}\, a^2\, c \quad (2)$$

The Scherrer diffraction formula is used to find the average particle sizes (D_{sh})

$$D_{sh} = \frac{k\lambda}{\beta \cos\theta} \quad (3)$$

Where k denotes a shape factor, λ indicates the X-ray wavelength, β signifies the full width at half maximum (FWHM), and θ indicates the Bragg angle.

The Scherrer method is commonly used to analyze diffraction peaks, which indicate the crystallographic orientation of a crystal. In the case of hematite, the (104) peak at 2θ = 33.14° reflects its preferential orientation. By determining the FWHM value of this peak, we can estimate the average crystallite size [17].

The X-ray density (ρ_x), bulk density (ρ_b) and porosity (% p) were obtained using the following equations [18]:

$$\rho_x = \frac{nM}{NV} \quad (4)$$

$$\rho_b = \frac{\text{Mass}}{\text{Volume}} \quad (5)$$

$$\%P = \left(1 - \frac{\rho_b}{\rho_x}\right) * 100 \quad (6)$$

Let n represent the number of atoms per unit cell, M denote the molecular weight, N signify Avogadro's number, and V indicate the volume of the unit cell.

The specific surface area (S), lattice strain (ε), and dislocation density (δ) were determined as follows [19, 20]:

$$S = \frac{6}{D * \rho_x} \quad (7)$$

$$\delta = \frac{1}{D^2} \quad (8)$$

$$\varepsilon = \frac{\beta}{4 \tan\theta} \quad (9)$$

Table 1: Lattice parameter (a, c), unit cell volume (V), crystallite size (D), dislocation density (δ), lattice strain (ε), specific surface area (S), x-ray density (ρ_x), bulk density (ρ_b), percentage of porosity at different pH levels (3,7, and 11).

pH	a (A°)	c (A°)	V (A°)^3	D (nm)	δ (nm^{-2}) 10^{-5}	e 10^{-4}	S (m^2/g)	ρ_x (g/cm^3)	ρ_b	P
3	5.0323	13.742	301.3794	82.07	14.85	14.79	41.544	1.7597	1.57708	11.57
7	5.0344	13.741	301.6090	61.48	26.45	19.75	55.495	1.7584	1.40792	24.89
11	5.0384	13.757	302.4402	65.77	23.12	18.48	52.021	1.7535	1.43542	22.15

These results indicate that pH affects the size of the crystals. Smaller crystals were produced when the pH was neutral (pH 7), while larger crystals were obtained under acidic conditions (pH 3). Furthermore, XRD data were employed to analyze the lattice strain measurements, which represent deviations in the lattice constants caused by crystal imperfections. As the crystal size decreased, the lattice strain increased [21]. Equation 8, which takes the crystal size into account, was used to get the dislocation density (δ). Due to their inverse relationship, it was found that the dislocation density increased as the crystal size decreased [22]. The X-ray density decreased as the pH increased, which depended on the unit cell volume. In addition, the atomic weight directly affects the X-ray density, which also varies with little variations in the unit cell volume. At pH 7, the bulk density was the lowest, whereas porosity and surface area were the highest. The samples exhibited low density and high porosity [23].

3.2 Vibrational characterization

Fourier-transform infrared spectroscopy was conducted to identify the functional groups of the synthesized α-Fe_2O_3 nanopowders. Figure 2(a-c) shows the obtained FTIR spectra of α-Fe_2O_3 nanoparticles at pH values of 3, 7, and 11, respectively. The presence of hematite nanoparticles can be verified by observing strong peaks below 600 cm^{-1}, which represent the stretching vibrations of the Fe-O bonds. FT-IR revealed two distinct peaks at 552 and 471 cm^{-1}, representing Fe-O bond vibrations in α-Fe_2O_3 [24]. The broad peak at 3437 cm^{-1} is attributed to the stretching vibrations of the (–OH) bond, as a result of the adsorbed water molecules on the surface of α-Fe_2O_3 nanoparticles [25], while the two sharp bands at 2924 cm^{-1} and 2855 cm^{-1} are due to the C-H stretching vibration of aliphatic hydrocarbons [26]. The peak at 2350 cm^{-1} may be related to (C=O) stretching in CO_2 [27]. The FTIR spectrum shows absorption bands at 1614 cm^{-1} and 1742 cm^{-1} corresponding to the stretching vibration of the aromatic (C=C) bonds in the ring and (C=O) bond, respectively [28, 29]. Furthermore, the band at 1366 cm^{-1} may be attributed to the bending vibration of the hydroxyl (OH) group in water [30, 31], and the absorption band at 1118 cm^{-1} is ascribed to the C-N bond of aliphatic amines or alcohols/phenols present in the rosemary leaf extract [32, 33].

3.3 Surface Morphology characterization

Field Emission Scanning Electron Microscopy (FE-SEM) was conducted to examine the morphology and surface characteristics of the synthesized hematite α-Fe_2O_3 nanoparticles. FE-SEM images of hematite α-Fe_2O_3 nanoparticles at different pH values (pH = 3, 7, and 11) are presented in Figure 3.

From the FE-SEM images, the hematite α-Fe_2O_3 nanoparticles were aggregated and exhibited a nanoplate-like morphology at a pH of 3, as illustrated in Figure 3(a). The hematite nanoparticles at pH 7 and 11 started to grow and transform into a semi-

spherical-like morphology, and the nanoparticles became clearer and more defined at pH 11. The pH-dependent morphology was

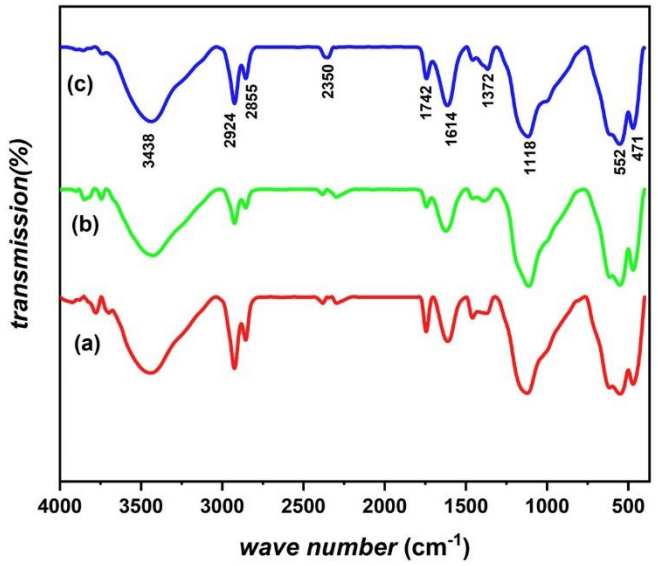

Figure 2: FT-IR spectra of synthesized α-Fe2O3 NPs at different pH values (a) pH = 3, (b) pH = 7, and (c) pH = 11.

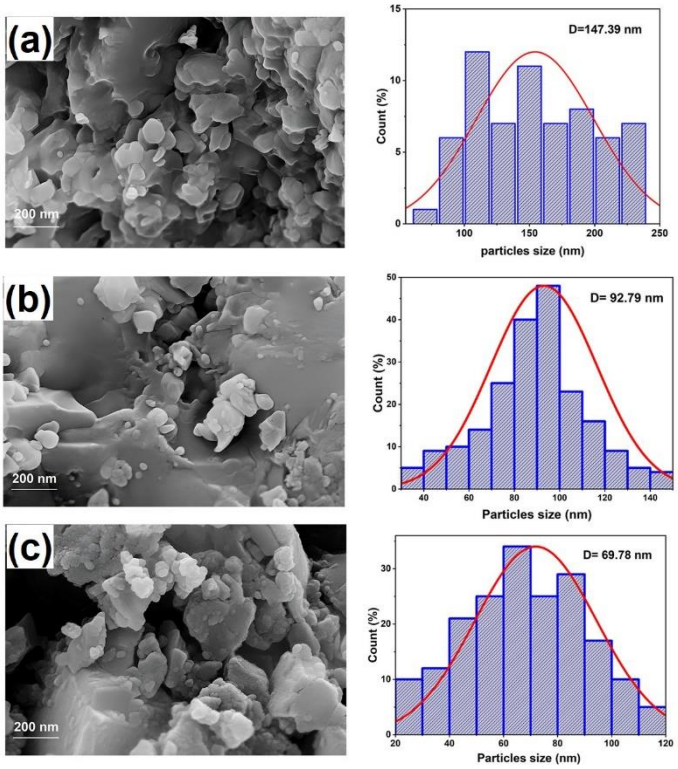

Figure 3: FE-SEM morphology of synthesized hematite α-Fe2O3 of different pH values (a) pH = 3, (b) pH = 7, and (c) pH = 11.

revealed by the FE-SEM images, and the hematite α-Fe_2O_3 NPs clearly appeared to be more regular and crystalline at high pH values, as shown in Figures 3(b, c). The shape transformation of hematite α-Fe_2O_3 is a function of pH which could be a reason for the good crystallinity of hematite α-Fe_2O_3.

The average particle size of hematite α-Fe_2O_3 nanoparticles was calculated for all samples using Image J software and was found to be about 147.39 nm, 92.79 nm, and 69.78 nm at pH values of 3, 7, and 11, respectively. The variation in particle size of the produced hematite α-Fe_2O_3 at different pH levels can be ascribed to the interaction between phenolic compounds and the surfaces of the Fe_2O_3 nanoparticles via hydrogen bonding as [34]. In the similar study, Abdullah et al. also showed that pH levels are an influence on the size and shape of iron oxide nanoparticles and demonstrated that by increasing the pH values, the particle size decreases [35].

3.4 Magnetic characterization

The magnetization hysteresis loops of the synthesized samples were measured using a vibrating sample magnetometer (VSM) to study the magnetic properties of the iron oxide nanoparticles. Figure 4 presents the VSM results (hysteresis loop) for the synthesized hematite α-Fe_2O_3 nanoparticles at different pH values (pH = 3, 7, and 11). The parameters obtained from the VSM curves are the magnetic saturation Ms, remanence magnetization Mr, and coercivity Hc, which are presented in Table 2. The obtained hysteresis loops of the synthesized samples reveal weak ferromagnetic behavior for all α-Fe_2O_3 NPs samples [36].

The obtained VSM results confirmed the benefits of changing the pH value during the synthesis of α-Fe_2O_3 NPs to preserve the magnetization properties of the iron oxide nanoparticles. The Ms values of α-Fe_2O_3 NPs were 0.292, 0.321, and 0.341 emu/g at pH values (pH = 3, 7, and 11) respectively. The α-Fe_2O_3 NPs at pH 7 and 11 preserved a magnetic saturation Ms higher than that at pH = 3, attributed to the hematite α-Fe_2O_3 NPs surfaces order/disorder interactions of the magnetic spin moment and the disturbance in the spinel structure inversion due to the Laplace pressure, as well as the increase in the weight and volume of the magnetite nanoparticles [37, 38]. Thus, an increase in the pH value (reduction in particle size) leads to an increase in the magnetic saturation Ms values. The low Ms value of hematite α-Fe_2O_3 clearly indicates that the obtained nanoparticles are nano-dimensional [39].

The magnetic saturation Ms value increased as the pH increased because of the decrease in the crystallite and particle sizes [40]. The results show that the hematite α-Fe_2O_3 NPs at different pH values have a unique magnetic performance owing to the particle size, shape, surface defect, single domain, crystal structure, and surface charge [41]. Bulk iron oxides demonstrate magnetic properties due to the presence of numerous domains in their structure, with each domain having spins aligned with the magnetic field and uniform magnetization being delineated by individual domain walls. The nanoscale dimensions of iron oxide exhibit a single domain, with spins orientated in the same direction as the applied magnetic field; thus, the coercivity H_c values decreased [42, 43]. See Figure 4 and Table 2.

Table 2: The VSM parameters of hematite α-Fe2O3 at different pH values.

pH	Ms (emu/g)	Mr (emu/g)	Hc (Oe)
3	0.292	0.084	2868
7	0.321	0.038	435
11	0.343	0.041	560

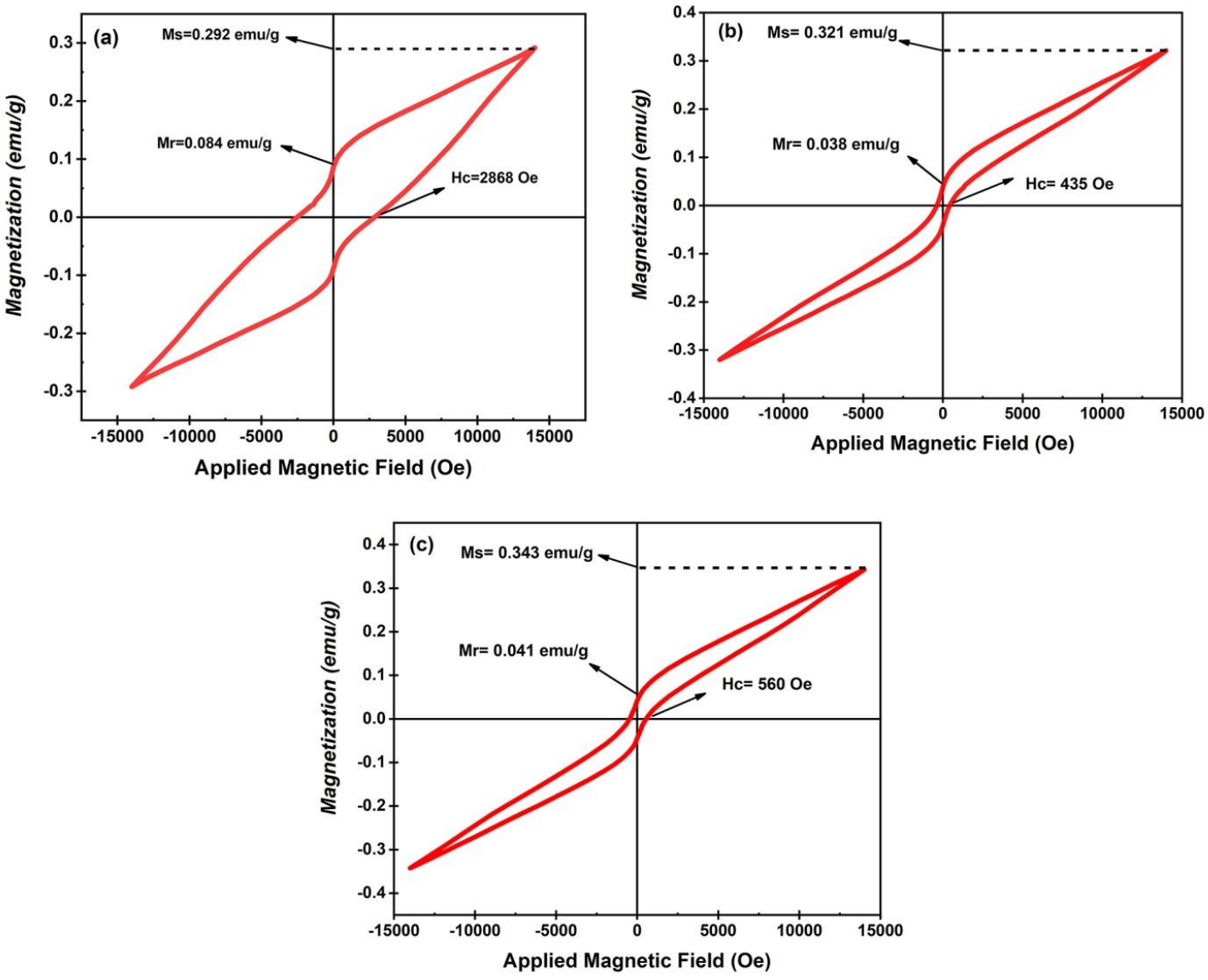

Figure 4: VSM results (hysteresis loop) for synthesized NPs of different pH values (a) pH = 3 (b) pH = 7 (c) pH = 11.

3.5 Dielectric characterization

This study investigated the dielectric properties, including the dielectric constant (ε'), dielectric loss factor (ε''), and AC conductivity (σ_{AC}), at various pH values at room temperature in the frequency range of 100 Hz to 2 MHz, as shown in Figure 5. The stored energy in a material is determined by the real part (ε') of the dielectric constant, which is calculated based on the capacitance using these formulas [44]:

$$\varepsilon' = \frac{C_p d}{A\varepsilon_o} \quad (10)$$

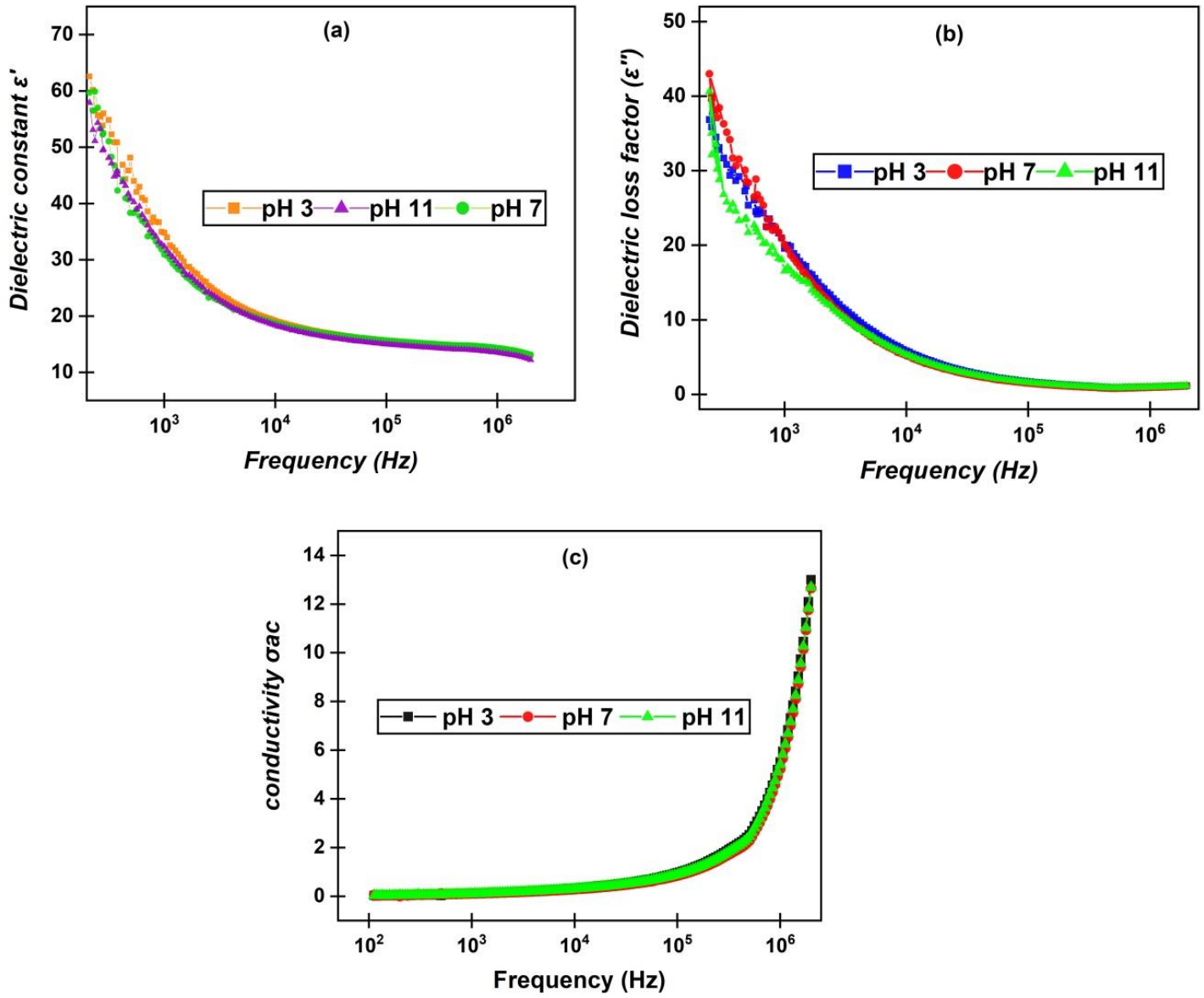

Figure 5: Variation of (a) Dielectric constant, (b) Dielectric loss, and (c) conductivity as a function of frequency at different pH values.

Where C_p represents capacitance, d denotes thickness, A signifies the area of the sample, and ε_o indicates the permittivity of free space, valued at 8.85 x 10^{-12} F/m.

As the frequency increases, the dielectric constant gradually decreases. However, in the high-frequency range, the dielectric constant remains constant across different pH levels. This behavior can be attributed to Koop's theory. At higher frequencies, the dielectric constant stabilizes and converges owing to reduced polarization and vacancy defects [45]. The energy loss is represented by the imaginary part of the dielectric constant ε'' and can be determined using the following formula [46]:

$$\varepsilon'' = \varepsilon' \tan \delta \quad (11)$$

Where tan δ denotes the dielectric loss angle (dissipation factor), which is measured directly using an LCR meter. The dielectric loss factor (ε'') was higher at lower frequencies and decreased as the frequency increased, eventually stabilizing at higher frequencies.

The AC conductivity (σ_{AC}) can be obtained from the following equation [47]:

$$\sigma_{AC} = 2\pi f \varepsilon_o \varepsilon' \tan \delta \quad (12)$$

Where f represents the frequency of the applied alternating current field.

The AC conductivity exhibited an interesting behavior with changing frequency. At higher frequencies, the conductivity reaches a maximum because of the presence of charge carriers and increased electron hopping [48]. The conductivity behavior of our samples can be explained using the electron hopping hypothesis. In this concept, the conductivity is mostly caused by the hopping of electrons between Fe^{2+} and Fe^{3+} ions present in the octahedral site [49]. This behavior aligns with the Maxwell-Wagner two-layer model, which suggests that conductivity gradually increases with frequency. However, the conductivity values tend to converge at lower frequencies, which could mean that the grains and grain boundaries within the samples were more active. At lower frequencies, fewer charge carriers are available, which means that electrons do not hop around as much, resulting in lower conductivity [50].

Conclusions

The eco-friendly green method was used to synthesize hematite α-Fe_2O_3 nanoparticles at different pH levels using plant extract. The produced nanoparticles were analyzed using XRD, FTIR, FESEM and VSM techniques, along with a study of their dielectric properties. From the XRD analysis, the nanopowders synthesized at pH 7 showed the smallest crystal size, highest surface area, and greatest porosity, whereas larger crystal sizes were obtained at an acidic pH of 3. Furthermore, with an increase in crystal size, the dislocation density and lattice strain increased. The smallest magnetic saturation and the largest coercivity were observed at pH 3. As the pH increased, magnetic saturation also increased.

Data Availability

All data generated or analyzed during this study are included in the article.

Conflicts of Interest

The authors declare that they have no conflicts of interest regarding the publication of this paper.

Acknowledgment

The authors are grateful to the Nanotechnology Research Laboratory, Department of Physics, University of Sulaimani, for their laboratory support.

References

[1] Khanzada, B., Akthar, N., Bhatti, M. Z., Ismail, H., Alqarni, M., Mirza, B., & Batiha, G. E. S. Green synthesis of gold and iron nanoparticles for targeted delivery: an in vitro and in vivo study. *J. Chem*, ***2021*****(1)**, 1581444 (2021).

[2] Mohamad, N. A. N., Arham, N. A., Jai, J., & Hadi, A. Plant extract as reducing agent in synthesis of metallic nanoparticles: a review. *Adv. Mat. Res*, **832**, 350-355 (2014).

[3] Jadoun, S., Arif, R., Jangid, N. K., & Meena, R. K. Green synthesis of nanoparticles using plant extracts: A review. *Environ. Chem. Lett*, **19(1)**, 355-374 (2021).

[4] Das, M., & Chatterjee, S. Green synthesis of metal/metal oxide nanoparticles toward biomedical applications: Boon or bane. In *Green synth, Charact. Appl. Nanopart*, (pp. 265-301). Elsevier (2019).

[5] Singh, J., Dutta, T., Kim, K. H., Rawat, M., Samddar, P., & Kumar, P. 'Green'synthesis of metals and their oxide nanoparticles: applications for environmental remediation. *J. nanobiotechnology*, **16**, 1-24 (2018).

[6] Nadaroglu, H., Güngör, A. A., & Ince, S. Synthesis of nanoparticles by green synthesis method. *INJIRR*, **1(1)**, 6-9 (2017).

[7] Aziz, W. J., Abid, M. A., Kadhim, D. A., & Mejbel, M. K. Synthesis of iron oxide (β-fe2o3) nanoparticles from Iraqi grapes extract and its biomedical application. In *IOP Conf. Ser.: Mater. Sci. Eng* (Vol. **881**, No. 1, p. 012099). IOP Publishing (2020, July).

[8] Sangaiya, P., & Jayaprakash, R. A review on iron oxide nanoparticles and their biomedical applications. *J. Supercond. Nov. Magn*, **31(11)**, 3397-3413 (2018).

[9] Montiel Schneider, M. G., Martín, M. J., Otarola, J., Vakarelska, E., Simeonov, V., Lassalle, V., & Nedyalkova, M. Biomedical applications of iron oxide nanoparticles: Current insights progress and perspectives. *Pharmaceut*, **14(1)**, 204 (2022).

[10] Sangaiya, P., & Jayaprakash, R. A review on iron oxide nanoparticles and their biomedical applications. *J. Supercond. Nov. Mag*, **31(11)**, 3397-3413 (2018).

[11] Tadic, M., Trpkov, D., Kopanja, L., Vojnovic, S., & Panjan, M. Hydrothermal synthesis of hematite (α-Fe2O3) nanoparticle forms: Synthesis conditions, structure, particle shape analysis, cytotoxicity and magnetic properties. *J. Alloys Compds*, **792**, 599-609 (2019)..

[12] Abbas, Z. M., Shatti, W. A., Mohammad, A. M., & Khodair, Z. T. Magnetic iron oxide: preparation and characterization for antibacterial activity applications. *J. Sol-Gel Sci. Technol.* **109**, 534-542. (2024).

[13] Saif, S., Tahir, A., & Chen, Y. Green synthesis of iron nanoparticles and their environmental applications and implications. *Nanomater*, **6(11)**, 209 (2016).

[14] Thakkar, K. N., Mhatre, S. S., & Parikh, R. Y. Biological synthesis of metallic nanoparticles. *NBM*, **6(2)**, 257-262 (2010).

[15] Narayanan, K. B., & Sakthivel, N.. Biological synthesis of metal nanoparticles by microbes. *Adv. Colloid Interface Sci*, **156(1-2)**, 1-13 (2010).

[16] Mote, V. D., Dargad, J. S., & Dole, B. N. Effect of Mn doping concentration on structural, morphological and optical studies of ZnO nano-particles. *Nanosci. Nanoengi*, **1(2)**, 116-122 (2013).

[17] Ilmi, M. M., Nurdini, N., Maryanti, E., Setiawan, P., & Ismunandar, I. X-ray diffraction peak profile for determination of microstructural properties of hematite (Fe2O3). *J. Res. Dev. Nano*, **1(1)**, 11-17 (2021).

[18] Saeed, Z., & Azhdar, B. A novel method for synthesizing narrow particle size distribution of holmium–doped strontium hexaferrite by sol-gel auto-combustion. *MRX*, **7(4)**, 045006 (2020).

[19] Hasan, S., & Azhdar, B. Thermo-dielectric, humidito-dielectric, and humidity sensing properties of barium monoferrite and barium hexaferrite nanoparticles. *Results Phys*, **42**, 105962 (2022).

[20] Basma, H., Rahal, H. T., & Awad, R. Enhancement of the magnetic properties of Ba1-xBixFe12O19 nanoparticles. *J. Magn. Magn. Mater*, **539**, 168413 (2021).

[21] Deshpande, S., Patil, S., Kuchibhatla, S. V., & Seal, S. Size dependency variation in lattice parameter and valency states in nanocrystalline cerium oxide. *Appl. Phys. Lett*, **87(13)**. (2005).

[22] Azhdar, B. Influence of fuel-to-oxidizer ratio, potential of hydrogen and annealing temperature on the structural and optical properties of nanocrystalline MgO powders synthesized by the hydrothermal method. *J. Exp. Nanosci* **18(1)**, 2276278 (2023).

[23] Hasan, S., & Azhdar, B. Effect of annealing temperature, annealing time, and hydrogen potential on the physical properties of Ni0. 5Zn0. 5Fe2O4 nanoparticles. *Ceram. Int*, **49(3)**, 5371-5381 (2023).

[24] Yoonus, J., Resmi, R., & Beena, B. Evaluation of antibacterial and anticancer activity of green synthesized iron oxide (α-Fe2O3) nanoparticles. *Mater. Today*, **46**, 2969-2974 (2021).

[25] Madubuonu, N., Aisida, S. O., Ali, A., Ahmad, I., Zhao, T. K., Botha, S., & Ezema, F. I. Biosynthesis of iron oxide nanoparticles via a composite of Psidium guavaja-Moringa oleifera and their antibacterial and photocatalytic study. *J. Photochem. Photobiol*, **199**, 111601 (2019).

[26] Venkateswarlu, S., Kumar, B. N., Prasad, C. H., Venkateswarlu, P., & Jyothi, N. V. V. Bio-inspired green synthesis of Fe3O4 spherical magnetic nanoparticles using Syzygium cumini seed extract. *Physica B Condens. Matter*, **449**, 67-71 (2014).

[27] Karmakar, R., Das, A. K., Pramanik, S., Kuiri, P. K., & Meikap, A. K. Tunable dielectric properties and magneto-dielectric coupling of hematite based trap free flexible semiconductor. *J. Alloys Compd.*, **881**, 160516 (2021).

[28] Wang, T., Jin, X., Chen, Z., Megharaj, M., & Naidu, R. Green synthesis of Fe nanoparticles using eucalyptus leaf extracts for treatment of eutrophic wastewater. *Sci. Total Environ*, **466**, 210-213 (2014).

[29] Salmani, M. H., Abedi, M., Mozaffari, S. A., Mahvi, A. H., Sheibani, A., & Jalili, M. Simultaneous reduction and adsorption of arsenite anions by green synthesis of iron nanoparticles using pomegranate peel extract. *J. environ. health sci. eng*, **19**, 603-612 (2021).

[30] Al-Hakkani, M. F., Gouda, G. A., Hassan, S. H., & Nagiub, A. M. Echinacea purpurea mediated hematite nanoparticles (α-HNPs) biofabrication, characterization, physicochemical properties, and its in-vitro biocompatibility evaluation. *J. Surf. Interfac*, **24**, 101113 (2021).

[31] Abdallah, Y., Ogunyemi, S. O., Abdelazez, A., Zhang, M., Hong, X., Ibrahim, E., ... & Chen, J. The green synthesis of MgO nano-flowers using Rosmarinus officinalis L.(Rosemary) and the antibacterial activities against Xanthomonas oryzae pv. oryzae. *Biomed Res. Int*, **2019(1)**, 5620989 (2019).

[32] Noukelag, S. K., Arendse, C. J., & Maaza, M. Biosynthesis of hematite phase α-Fe2O3 nanoparticles using an aqueous extract of Rosmarinus officinalis leaves. *Mater. Today*, **43**, 3679-3683 (2021).

[33] Noukelag, S. K., Mohamed, H. E. A., Moussa, B., Razanamahandry, L. C., Ntwampe, S. K. O., Arendse, C. J., & Maaza, M. Investigation of structural and optical properties of biosynthesized Zincite (ZnO) nanoparticles (NPs) via an aqueous extract of Rosmarinus officinalis (rosemary) leaves. *MRS Adv*, **5(45)**, 2349-2358 (2020).

[34] Salgado, P., Márquez, K., Rubilar, O., Contreras, D., & Vidal, G. The effect of phenolic compounds on the green synthesis of iron nanoparticles (Fe x O y-NPs) with photocatalytic activity. *Appl. Nanosci*, **9**, 371-385 (2019).

[35] Abdullah, J. A. A., Díaz-García, Á., Law, J. Y., Romero, A., Franco, V., & Guerrero, A. Sustainable nanomagnetism: investigating the influence of green synthesis and ph on iron oxide nanoparticles for enhanced biomedical applications. *Polym*, **15(18)**, 3850 (2023).

[36] Rufus, A., Sreeju, N., Vilas, V., & Philip, D. Biosynthesis of hematite (α-Fe2O3) nanostructures: size effects on applications in thermal conductivity, catalysis, and antibacterial activity. *J. Mol. Liq.*, **242**, 537-549 (2017).

[37] Nedkov, I., Kolev, S., Zadro, K., Krezhov, K., & Merodiiska, T. Crystalline anisotropy and cation distribution in nanosized quasi-spherical ferroxide particles. *J. Magn. Magn. Mater*, **272**, E1175-E1176 (2004).

[38] Segovia, L. C. A., Agudelo, J. I. D., Glisoni, R. J., Acha, C., De Zan, M. M., & Rintoul, I. A multiparametric model for the industrialization of co-precipitation synthesis of nano-commodities. *Nanotechnol*, **31(18)**, 185604 (2020).

[39] Riaz, S., Shah, S. Z. H., Kayani, Z. N., & Naseem, S. Magnetic and structural phase transition in iron oxide nanostructures. *Mater. Today*, **2(10)**, 5280-5287 (2015).

[40] Wu, J., Mao, S., Ye, Z. G., Xie, Z., & Zheng, L. Room-temperature weak ferromagnetism induced by point defects in α-Fe2O3. *ACS Appl. Mater. Interfaces*, **2(6)**, 1561-1564 (2010).

[41] Vallina, B., Rodriguez-Blanco, J. D., Brown, A. P., Benning, L. G., & Blanco, J. A. Enhanced magnetic coercivity of α-Fe 2 O 3 obtained from carbonated 2-line ferrihydrite. *J. Nanoparticle Res*, **16**, 1-13 (2014).

[42] Zong, Y., Sun, Y., Meng, S., Wang, Y., Xing, H., Li, X., & Zheng, X. Doping effect and oxygen defects boost room temperature ferromagnetism of Co-doped ZnO nanoparticles: experimental and theoretical studies. *RSC Adv*, **9(40)**, 23012-23020 (2019).

[43] Sayed, F. N., & Polshettiwar, V. Facile and sustainable synthesis of shaped iron oxide nanoparticles: effect of iron precursor salts on the shapes of iron oxides. *Sci. Rep*, **5(1)**, 9733 (2015).

[44] Anand, S., Vinosel, V. M., Jenifer, M. A., & Pauline, S. Dielectric properties, ac electrical conductivity and electric modulus profiles of hematite (α-Fe2O3) nanoparticles. *Int. Res. J. Eng. Technol.*, **4(9)**, 358-362 (2017).

[45] Archana, V., Joseph Prince, J., & Kalainathan, S. Simple One-Step Leaf Extract-Assisted Preparation of α-Fe2O3 Nanoparticles, Physicochemical Properties, and Its Sunlight-Driven Photocatalytic Activity on Methylene Blue Dye Degradation. *J. Nanomater*, **2021(1)**, 8570351 (2021).

[46] Kuekha, R., Mubarak, T. H., & Azhdar, B. Synthesis, structural, magnetic, and dielectric properties of Ni2+, Mn2+ Co-substituted CoFe2O4 nanoferrites using sol–gel auto combustion method. *Mater. Sci. Eng. A: B*, **292**, 116411 (2023).

[47] Hasan, S., & Azhdar, B. NiFe2O4 and ZnFe2O4 nanoparticles synthesis by sol-gel auto-combustion for humidity sensor applications. *J. Sol-Gel Sci. Technol*, **105(2)**, 416-429 (2023).

[48] Gowreesan, S., & Ruban Kumar, A. Structural, magnetic, and electrical property of nanocrystalline perovskite structure of iron manganite (FeMnO 3). *Appl. Phys. A*, **123**, 1-8 (2017).

[49] Hasan, S., & Azhdar, B. Synthesis and investigation of structural, elastic, and electrical properties of cobalt and magnesium substituted Ni–Zn spinel ferrite nanoparticles. *J. Condens. Matter Phys*, ***35*(42)**, 425303 (2023).

[50] Sharma, S., Basu, T., Shahee, A., Singh, K., Lalla, N. P., & Sampathkumaran, E. V. Complex dielectric and impedance behavior of magnetoelectric Fe2TiO5. *J. Alloys Compd*, **663**, 289-294 (2016).